PHYSICAL REVIEW B **95**, 064205 (2017)

Mode mixing induced by disorder in a graphene *pnp* junction in a magnetic field

Ning Dai[1] and Qing-Feng Sun[1,2,*]

[1] *International Center for Quantum Materials, School of Physics, Peking University, Beijing 100871, China*

[2] *Collaborative Innovation Center of Quantum Matter, Beijing 100871, China*

(Received 23 November 2016; revised manuscript received 21 January 2017; published 15 February 2017)

We study the electron transport through the graphene *pnp* junction under a magnetic field and show that mode mixing plays an essential role. By using the nonequilibrium Green's function method, the space distribution of the scattering state for a specific incident mode as well the elements of the transmission and reflection coefficient matrices are investigated. All elements of the transmission (reflection) coefficient matrices are very different for a perfect *pnp* junction, but they are the same at a disordered junction due to the mode mixing. The space distribution of the scattering state for the different incident modes also exhibits similar behaviors, i.e., that they distinctly differ from each other in the perfect junction but are almost the same in the disordered junction. For a unipolar junction, when the mode number in the center region is less than that in the left and right regions, the fluctuations of the total transmission and reflection coefficients are zero, although each element has a large fluctuation. These results clearly indicate the occurrence of perfect mode mixing and play an essential role in a graphene *pnp* junction transport.

DOI: 10.1103/PhysRevB.95.064205

I. INTRODUCTION

Graphene, a monolayer carbon hexagon lattice, has received much attention in recent years for its novel electronic properties. Its conduction band and valence band are only consisted of π bonds under the effect of sp^2 hybridization. In pristine graphene, conduction and valence bands contact exactly on the Fermi surface at the corners of the Brillouin zone, and form linear Dirac cones [1]. This linear dispersion leads to a high carrier mobility and makes carriers obey the massless Dirac equation, which usually occurs in quantum electro-dynamics [2]. Thus, graphene presents some relativistic properties such as Klein tunneling [3]. When an intense magnetic field perpendicularly exerts on the graphene plane, graphene presents an anomalous integer quantum Hall effect with its Hall plateaus at the half-integer value $4(n + 1/2)e^2/h$, where the number 4 is from the spin and valley degeneracy.

The high carrier mobility and tunable band structure of graphene make it a promising candidate of new electronic material [4]. Nowadays, various electronic components have been fabricated of graphene, such as switch [5], *pn* junction [6], transistor [7,8], and even integrated circuit [9]. As an elementary building block of other electronic components, the graphene *pn* junction has invoked great interest. In many schemes, it is constructed on a graphene stripe, which is divided into two regions with Fermi energy tuned differently [10,11]. Some attractive prediction of a graphene *pn* junction has been reported. For example, a sharp graphene *pn* junction can focus electrons emitted from one point source [12]. On the other hand, a smooth *pn* junction transmits only those carriers whose momenta are almost perpendicular to the *pn* interface [13]. When a perpendicular magnetic field is applied, some snake states zigzag along the *pn* interface [14–18].

The *pnp* junction is consisted of two *pn* junctions arranged back to back. In many schemes, graphene *pnp* junction is built of a graphene nanoribbon, with a top gate and back gates controlling the carrier type and density in the emitter region, central base region, and collector region [19–23]. For example, Nam *et al.* designed a high-quality graphene *pnp* device using a local gate to tune the central base region, and a global gate to tune both collector and emitter regions [24,25]. Furthermore, a graphene *pnp* junction has also been fabricated chemically, of which energy band is tuned by substrate [26] or doping [27,28].

There have been many works on transport properties of graphene *pnp* junctions. For example, this device is an appropriate platform to study Klein tunneling, where a conductance oscillation due to Fabry-Perot interference would appear under some particular condition [22,29], and it can act as a Veselago lens or beam splitter by the advantage of electrons focusing property of a graphene *pn* junction [12,30].

When a vertical strong magnetic field is applied on a graphene *pn* or *pnp* junction, drifting electrons gather at the edge of each region under the effect of Lorenz force. Therefore, edge modes in each region act as conducting channels and carriers travel along the *pn* interface. Because electron (*n* region) and hole (*p* region) suffer opposite Lorenz force, the propagating direction is the same in both the *p* region and *n* region at *pn* interface. These boundary states at *pn* interface will mix up in the presence of disorder, and such mixing will also happen among the edge modes [31]. The degree of mixing affects the magnitude conductance. Under the assumption of complete mixing, the conductance of *pn* or *pnp* junction can be achieved. In the case of a *pn* junction, in the unipolar regime where the filling factor ν_1 holds the same sign of the filling factor ν_2 sign, the conductance $g = \min\{|\nu_1|,|\nu_2|\}$, and in bipolar regime where ν_1,ν_2 hold different signs, $g = \frac{|\nu_1||\nu_2|}{|\nu_1|+|\nu_2|}$ [32]. These predictions have been supported by a number of experiments [6,11,23], as soon as they were put forward. Soon after, it was verified by numerical simulation [33]. The conductance of a *pnp* junction has also been analytically given and certified by many experiments [25,34–36], and we will present the expressions of the conductance in Sec. III.

However, these expressions of the conductance are based on a hypothesis that all the modes are completely mixed. In fact,

---

[*] sunqf@pku.edu.cn

it has been verified that without mode mixing the conductance is smaller than the case with fully mixed modes. For example, Morikawa *et al.* fabricated an ultraclean graphene *npn* junction with h-BN dielectrics, in which the disorder-induced mode mixing was strongly suppressed [37], In high magnetic fields, this device acted as a built-in Aharonov-Bohm interferometer, whose two-terminal conductance oscillates with magnetic field, compared with the conductance plateau in the fully mixed case [25,34–36]. These experiments highlight the significance of disorder for mode mixing. However, although there has been some work on the effect of disorder in a graphene *pn* junction [38–41], systematic research for mode mixing procedure in a graphene *pnp* junction is still lacking, which is carried out in this paper.

In this paper, we study the space distribution of the scattering wave function and the current density, as well the transmission and reflection coefficient matrices in a graphene *pnp* junction. Sanvito and Lambert have developed a method to solve the transmission coefficient matrix in a two-terminal scattering system [42]. Here, we extend its application to the multiterminal system, and the primitive cell of each terminal can be multiple layers. Furthermore, the formulas of the reflection coefficient matrix as well the scattering wave function in the real space are derived. With the help of these formulas, we carry out a series of numerical investigations on the electron transport through a graphene *pnp* junction. For a perfect *pnp* junction, the elements of the transmission and reflection coefficient matrices are very different, and the space distribution of the scattering wave function for different incident modes has a large difference as well. However, for a disordered *pnp* junction in which the disorder is stronger than a critical value, all elements of the transmission (reflection) matrix are the same regardless of unipolar or bipolar junctions, so are the scattering wave functions for different incident modes. This clearly indicates the occurrence of perfect mode mixing. In addition, the mode mixing process is relevant to the intensity of the magnetic field and disorder nature. For a unipolar *pnp* junction, while the mode number in the center region is less than that in the left and right regions, all elements of transmission and reflection matrices have large fluctuations, although the fluctuation of the sum of all elements is exactly zero. This means that the mode mixing occurs in this case also.

The rest of this paper is organized as follows. In Sec. II, based on the nonequilibrium Green's function method, we derive the expressions of the reflection amplitude and transmission amplitude for the incident electron from a specific mode in the multiterminal scattering system. In Sec. III, these expressions are applied in a graphene *pnp* junction to reveal the mode mixing process. Finally, the results are summarized in Sec. IV.

II. MODEL AND METHOD

We consider a multiterminal scattering system as shown in Fig. 1(a). The crucial physical quantities for the scattering problem are the reflection amplitude $r_{j\beta,l\beta}$ and transmission amplitude $t_{j\alpha,l\beta}$, in which $t_{j\alpha,l\beta}$ describes the amplitude of the outgoing electron at the mode j in the terminal α for the incident electron from the mode l in the terminal β, and $r_{j\beta,l\beta}$ is the amplitude of the reflection electron at the mode j in the same terminal β. In this section, we deduce the formula of the reflection amplitude and transmission amplitude by using the nonequilibrium Green's function method. About two decades ago, Sanvito and Lambert developed a Green's function method to solve the transmission amplitude in a two-terminal device [42]. However, this method is under a strong restriction in the form of Hamiltonian of the terminals, i.e., that the matrix of the hopping Hamiltonian is required to be invertible. Here, we relax this restriction and expand its application in the case of a multiterminal system. In addition, the expression of reflection amplitude is derived also.

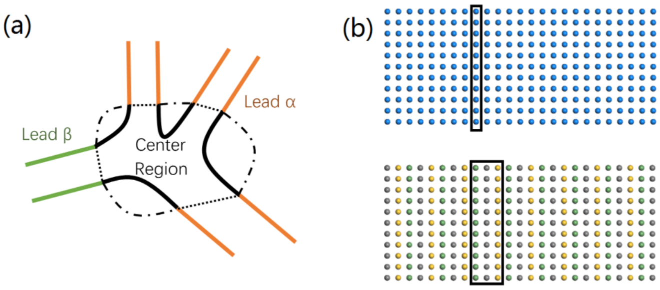

FIG. 1. (a) Schematic of a multiterminal scattering system. The center scattering region is connected to an injecting lead (lead β) and several outgoing leads (lead α). (b) Wires with primitive cell consisted of a simple layer (upper) and multiple layers (lower). Suppose the Hamiltonian between each of the two adjacent layers is invertible. A primitive cell in the upper wire contains only one layer, so that the Hamiltonian H_1 between two adjacent primitive cells is invertible. However, the Hamiltonian H_1 is noninvertible in the lower wire whose primitive cell contains multiple layers.

In the tight-binding representation, the Hamiltonian of the multiterminal scattering device [see Fig. 1(a)] consisting of the center scattering region connecting with several leads is

$$H = \sum_{i} \epsilon_i a_i^{\dagger} a_i + \sum_{i,j} t_{ij} a_i^{\dagger} a_j, \tag{1}$$

where a_i $(a_j^{\dagger})$ is the annihilation (creation) operator on the site i. Here, the leads are assumed to be perfect and without scattering. The transport can be described by a pure scattering state when the system length scale is small compared to elastic mean-free path or phase-relaxation length. Suppose a Bloch wave $e^{ik_{l\beta}z}\phi^{(l\beta)}$ injects to the center scattering region from the mode l in the lead β, and then is scattered into other leads. The scattering state $\psi^{(l\beta)}$ takes the form of the following equation:

$$\psi^{(l\beta)}(z) = \begin{cases} \phi^{(l\beta)} \frac{e^{ik_{l\beta}z}}{\sqrt{v_{l\beta}}} + \sum_j r_{j\beta,l\beta} \bar{\phi}^{(j\beta)} \frac{e^{i\bar{k}_{j\beta}z}}{\sqrt{v_{j\beta}}} & \text{lead} : \beta, \\ \sum_j t_{j\alpha,l\beta} \phi^{(j\alpha)} \frac{e^{ik_{j\alpha}z}}{\sqrt{v_{j\alpha}}} & \text{lead} : \alpha \neq \beta. \end{cases} \tag{2}$$

The coordinate z is the index of the primitive cell in the lead and it is set according to the following rules: in injecting lead (labeled by β), the lead starts from the center scattering region where $z = 0$, and then extends to infinity denoted by $z = -\infty$; in other leads, each lead starts at $z = 0$ and then extends to $z = \infty$. The indices l and j here indicate a different mode in an infinite wire. Wave function and wave vector transporting along the $+z$ axis are denoted by ϕ and k, while the opposites are denoted by $\bar{\phi}$ and $\bar{k}$. $t_{j\alpha,l\beta}$ and $r_{j\beta,l\beta}$ are the transmission and reflection amplitudes which are the crucial physical quantities to be solved below. After $t_{j\alpha,l\beta}$ and $r_{j\beta,l\beta}$ are solved, the transmission coefficient from the lead β to the lead α is $T_{\alpha\beta} = \sum_{j,l} |t_{j\alpha,l\beta}|^2$, and the conductance can be obtained from the Landauer-Büttiker formula straightforwardly [43].

Next, we solve the wave functions ($\phi^{(l\alpha)}$ and $\bar{\phi}^{(l\alpha)}$) and wave vectors ($k_{l\alpha}$ and $\bar{k}_{l\alpha}$) of a specific lead α. For the sake of simplicity, the index α is omitted in the rest of this paper. Consider an infinite lead, which can be viewed as a periodical arrangement of primitive cells [see Fig. 1(b)]. Its Hamiltonian can be expressed in the form of a block matrix according to the primitive cell, and the Schrödinger equation is

$$\begin{bmatrix} \ddots & & & & \\ & H_1^\dagger & H_0 - E & H_1 & & \\ & & H_1^\dagger & H_0 - E & H_1 & \\ & & & & & \ddots \end{bmatrix} \begin{bmatrix} \vdots \\ \phi(z) \\ \phi(z+1) \\ \vdots \end{bmatrix} = 0, \tag{3}$$

where H_0 denotes a Hamiltonian within a single cell, and H_1 denotes a Hamiltonian between two adjacent cells. The wave function is denoted by coordinate index z. Further, the Bloch theorem preserves $\phi(z) = e^{ikz}\phi$.

In the previous work by Sanvito and Lambert [42], the hopping matrix H_1 was required to be invertible. Here, we expand to noninvertible H_1. Suppose the primitive cell can be divided into n layers, and the hopping matrix between every adjacent layers is invertible [see Fig. 1(b)]. The modified method can apply in this situation even if the whole H_1 between two adjacent primitive cells is not invertible. In this case, the matrix in Eq. (3) can be substituted by

$$H_0 = \begin{bmatrix} h_{11} & h_{12} & 0 & \dots & 0 \\ \vdots & & & & \vdots \\ \dots & h_{i-1,i}^\dagger & h_{ii} & h_{i,i+1} & \dots \\ \vdots & & & & \vdots \\ 0 & \dots & 0 & h_{n-1,n}^\dagger & h_{nn} \end{bmatrix},$$

$$H_1 = \begin{bmatrix} 0 & \dots & 0 \\ \vdots & \ddots & \vdots \\ h_{n1} & \dots & 0 \end{bmatrix}, \tag{4}$$

$$\phi(z) = [\phi_1(z), \dots, \phi_n(z)]^{\mathrm{T}},$$

where h_{ii} and $h_{i,i+1}$ are the Hamiltonian of the ith layer and the hopping Hamiltonian between the ith and $(i+1)$th layers. Here, all the h_{ij} are invertible, although H_1 is noninvertible. $\phi_i(z)$ is the wave function at the ith layer in the cell z. Substituting Eq. (4) and Bloch wave $\phi(z) = e^{ikz}\phi$ into Eq. (3), we have

$$\begin{bmatrix} h_{11} - E & h_{12} & 0 & \dots & e^{-ik}h_{n1}^\dagger \\ \vdots & & & & \vdots \\ \dots & h_{i-1,i}^\dagger & h_{ii} - E & h_{i,i+1} & \dots \\ \vdots & & & & \vdots \\ e^{ik}h_{n1} & \dots & 0 & h_{n-1,n}^\dagger & h_{nn} - E \end{bmatrix} \begin{bmatrix} \phi_1 \\ \vdots \\ \phi_i \\ \vdots \\ \phi_n \end{bmatrix} = 0 \tag{5}$$

and an equation of Bloch vector k is acquired:

$$\begin{vmatrix} h_{11} - E & h_{12} & 0 & \dots & e^{-ik}h_{n1}^\dagger \\ \vdots & & & & \vdots \\ \dots & h_{i-1,i}^\dagger & h_{ii} - E & h_{i,i+1} & \dots \\ \vdots & & & & \vdots \\ e^{ik}h_{n1} & \dots & 0 & h_{n-1,n}^\dagger & h_{nn} - E \end{vmatrix} = 0. \tag{6}$$

This is a rational expression equation of $x = e^{ik}$ whose highest order is N and lowest order is $-N$, so there are $2N$ roots in total, where N is the number of atoms in each layer as well as the dimension of each matrix block. Moreover, the Hermiticity of this matrix guarantees that if vector k satisfies the equation, k^* satisfies as well. This results in a balance between leftward states and rightward states which can be seen if an infinitesimal imaginary number $i0^+$ is added on the eigenenergy E: According to $k \sim E$ relation $dk = \frac{dE}{\hbar v_k}$, those leftward k ($v_k > 0$) hold a positive infinitesimal imaginary part, while the rightward ($v_k < 0$) hold a negative one. For this reason, every leftward mode, both evanescent (whose k hold a positive finite imaginary part) and transporting (whose k hold a positive infinitesimal imaginary part) have its conjugate rightward counterpart.

In order to acquire all possible wave vectors k and wave functions ϕ in Eq. (5), the transition matrix is introduced:

$$t_i = \begin{bmatrix} 0 & 1 \\ -h_{i,i+1}^{-1}h_{i-1,i}^\dagger & -h_{i,i+1}^{-1}(h_{ii} - E) \end{bmatrix}. \tag{7}$$

It can be simply deduced from Eqs. (3) and (4) that

$$\begin{aligned} t_1 \begin{bmatrix} \phi_n(z-1) \\ \phi_1(z) \end{bmatrix} &= \begin{bmatrix} \phi_1(z) \\ \phi_2(z) \end{bmatrix}, \\ t_i \begin{bmatrix} \phi_{i-1}(z) \\ \phi_i(z) \end{bmatrix} &= \begin{bmatrix} \phi_i(z) \\ \phi_{i+1}(z) \end{bmatrix}, \\ t_n \begin{bmatrix} \phi_{n-1}(z) \\ \phi_n(z) \end{bmatrix} &= \begin{bmatrix} \phi_n(z) \\ \phi_1(z+1) \end{bmatrix}. \end{aligned} \tag{8}$$

The transition matrix T_i is defined as $T_i = t_{i-1} \dots t_1 t_n \dots t_i$, thus, we get

$$T_i \begin{bmatrix} \phi_{i-1}(z) \\ \phi_i(z) \end{bmatrix} = \begin{bmatrix} \phi_{i-1}(z+1) \\ \phi_i(z+1) \end{bmatrix} = e^{ik} \begin{bmatrix} \phi_{i-1}(z) \\ \phi_i(z) \end{bmatrix}. \tag{9}$$

On the one hand, Eq. (9) shares the same solution k and ϕ with Eq. (5). On the other hand, Eq. (9) is an eigenvalue equation, and the eigenvalues e^{ik} and eigenfunctions can be easily solved. As we have analyzed before, with a infinitesimal imaginary number $i0^+$ added on the eigenenergy E, T_i have N eigenvalues that $|e^{ik}| < 1$ indicating leftward wave vectors and N corresponding rightward with $|e^{ik}| > 1$. The transporting modes can be distinguished from those evanescent modes because for transporting modes $|e^{ik}| \simeq 1$, while for evanescent modes $|e^{ik}|$ hold a certain deviation from 1. Sorting all eigenfunctions $[\begin{smallmatrix} \phi_{i-1} \\ \phi_i \end{smallmatrix}]$ into a matrix by the ascending order of $|e^{ik}|$, we have

$$T_i \begin{bmatrix} \Phi_{L,i-1} & \Phi_{R,i-1} \\ \Phi_{Li} & \Phi_{Ri} \end{bmatrix} = \begin{bmatrix} \Phi_{L,i-1} & \Phi_{R,i-1} \\ \Phi_{Li} & \Phi_{Ri} \end{bmatrix} \begin{bmatrix} \chi_L & 0 \\ 0 & \chi_R \end{bmatrix}. \tag{10}$$

χ_L (χ_R) is a diagonal matrix, whose diagonal is arranged by the ascending order of all e^{ik} ($e^{i\bar{k}}$). The wave functions ϕ ($\bar{\phi}$) of all modes exist in corresponding matrices Φ_{Li} and Φ_{Ri}:

$$\chi_L = \begin{bmatrix} e^{ik_1} & & 0 \\ & \ddots & \\ 0 & & e^{ik_N} \end{bmatrix}, \quad \chi_R = \begin{bmatrix} e^{i\bar{k}_1} & & 0 \\ & \ddots & \\ 0 & & e^{i\bar{k}_N} \end{bmatrix}, \tag{11}$$

and

$$\Phi_{Li} = \left[\phi_i^{(1)}, \ldots, \phi_i^{(N)}\right], \quad \Phi_{Ri} = \left[\bar{\phi}_i^{(1)}, \ldots, \bar{\phi}_i^{(N)}\right]. \tag{12}$$

After solving the wave functions ϕ ($\bar{\phi}$) and wave vectors k ($\bar{k}$), the surface Green's function of the lead can be obtained straightforwardly. Suppose the lead is leftward infinite and truncated at the ith layer of cell 0, the surface Green's function is

$$G^r_{\text{surf}} = \begin{cases} \left(1 - \Phi_{Rn}\chi_R^{-1}{\Phi_{R1}}^{-1}\Phi_{L1}\chi_L{\Phi_{Ln}}^{-1}\right)/V_n & \text{for } i = 1, \\ (1 - \Phi_{R,i-1}{\Phi_{Ri}}^{-1}\Phi_{Li}{\Phi_{L,i-1}}^{-1})/V_{i-1} & \text{for } i = 2\ldots n, \end{cases} \tag{13}$$

where

$$V_i = \begin{cases} h^\dagger_{n1}\left(\Phi_{Ln}\chi_L^{-1}{\Phi_{L1}}^{-1} - \Phi_{Rn}\chi_R^{-1}{\Phi_{R1}}^{-1}\right) & \text{for } i = 1, \\ h^\dagger_{i-1,i}(\Phi_{L,i-1}{\Phi_{Li}}^{-1} - \Phi_{R,i-1}{\Phi_{Ri}}^{-1}) & \text{for } i = 2\ldots n. \end{cases} \tag{14}$$

Next, we solve the transmission amplitude $t_{j\alpha,l\beta}$ and reflection amplitude $r_{j\beta,l\beta}$ with the help of nonequilibrium Green's function. The Green's function G^r_{sys} has been obtained in previous references [44]. The Green's function of the whole system G^r_{sys} is defined from the equation $(E - H)G^r_{\text{sys}}(z,i;z',i') = \delta_{zz'}\delta_{ii'}\mathbf{1}$. Notice that the scattering state $\psi^{(l\beta)}$ in Eq. (2) satisfies the Schrödinger equation $(E - H)\psi^{(l\beta)}(z,i) = 0$, which is similar with the definition of G^r_{sys} except at $z = z'$ and $i = i'$. So, we can structure the Green's function by using the scattering state $\psi^{(l\beta)}$:

$$G^r_{\text{sys}}(z,i;z',i') = \begin{cases} \Phi_{Li\alpha}\chi_{L\alpha}^{z-z'}{\sqrt{v_{L\alpha}}}^{-1}t_{\alpha,\beta}\sqrt{v_{L\beta}}{\Phi_{Li'\beta}}^{-1}V^{-1}_{i'\beta}, & z \text{ in the lead } \alpha \\ \Phi_{Li\beta}\chi_{L\beta}^{z-z'}{\Phi_{Li'\beta}}^{-1}V^{-1}_{i'\beta} + \Phi_{Ri\beta}\chi_{R\beta}^{z-z'}{\sqrt{v_{R\beta}}}^{-1}r_{\beta,\beta}\sqrt{v_{L\beta}}{\Phi_{Li'\beta}}^{-1}V^{-1}_{i'\beta}, & z > z' \text{ or } z = z' \text{ with } i \geqslant i' \text{ in the lead } \beta \\ \Phi_{Ri\beta}\chi_{R\beta}^{z-z'}{\Phi_{Ri'\beta}}^{-1}V^{-1}_{i'\beta} + \Phi_{Ri\beta}\chi_{R\beta}^{z-z'}{\sqrt{v_{R\beta}}}^{-1}r_{\beta,\beta}\sqrt{v_{L\beta}}{\Phi_{Li'\beta}}^{-1}V^{-1}_{i'\beta}, & z < z' \text{ or } z = z' \text{ with } i \leqslant i' \text{ in the lead } \beta. \end{cases} \tag{15}$$

Here, we explain some notation in Eq. (15). (z,i) indicates the field layer in Green's function, where z denotes the primitive cell and i denotes the layer in cell, and (z',i') indicates the source layer. The source layer is fixed in the incident lead β. Here, $\Phi_{Li\beta}, \Phi_{Ri\beta}, \chi_{L\beta}, \chi_{R\beta}, v_{L\beta}, v_{R\beta}$ and the reflection amplitude $r_{\beta,\beta}$ all are the matrix with the dimension $N_\beta \times N_\beta$, the transmission amplitude $t_{\alpha,\beta}$ is a matrix with the dimension $N_\alpha \times N_\beta$. v_L is a diagonal matrix of velocity v_{k_l}, which can be acquired by

$$v_{k_l} = \frac{i}{\hbar}\langle\phi_l|H_1 e^{ik_l} - H_1^\dagger e^{-ik_l}|\phi_l\rangle \tag{16}$$

and v_R is its rightward counterpart.

From Eq. (15), taking z at the lead α, the transmission amplitude matrix $t_{\alpha,\beta}$ can be deduced:

$$t_{\alpha,\beta} = \sqrt{v_{L\alpha}}\chi_{Li\alpha}^{z'-z}{\Phi_{Li\alpha}}^{-1}G^r_{\text{sys}}(z,i;z',i')V_{i'\beta}\Phi_{Li'\beta}{\sqrt{v_{L\beta}}}^{-1}. \tag{17}$$

Taking $z = z'$ at the lead β, the reflection amplitude matrix $r_{\beta,\beta}$ can be obtained:

$$r_{\beta,\beta} = \sqrt{v_{R\beta}}{\Phi_{Ri\beta}}^{-1}\left[G^r_{\text{sys}}(z,i;z,i) - V^{-1}_{i\beta}\right]V_{i\beta}\Phi_{Li\beta}{\sqrt{v_{L\beta}}}^{-1}. \tag{18}$$

Technically, evanescent modes which hold a complex velocity v can be replaced by a 0 in matrix $v_{L/R}$ and $v^{-1}_{L/R}$, ensuring that only transporting modes remain. After obtaining the transmission and reflection amplitudes, the transmission and reflection coefficients $T_{\alpha j,\beta l} = |t_{\alpha j,\beta l}|^2$ and $R_{\beta j,\beta l} = |r_{\beta j,\beta l}|^2$.

Comparing Eqs. (2) and (15), the scattering wave function Ψ_β in the whole system can be obtained also:

$$\Psi_\beta(z,i) = G^r_{\text{sys}}(z,i;z',i')V_{i'\beta}\Phi_{Li'\beta}, \tag{19}$$

where z is required to be larger than z'. The matrix Ψ_β can be written as

$$\Psi_\beta = \left[\psi^{(1\beta)}, \ldots, \psi^{(N\beta)}\right], \tag{20}$$

and $\psi^{(l\beta)}$ is the scattering wave function in the whole system (including the center scattering region) for the incident electron from the lead β at the mode l. After obtaining the scattering wave function, the current density $j^{(l\beta)}$ for a specific incident mode can be solved straightforwardly.

III. RESULTS AND DISCUSSIONS

In this section, we employ the above method to investigate mode mixing in a graphene *pnp* junction. This is a two-terminal system and the center scattering region is a *pnp* junction as shown in Fig. 2. The Hamiltonian of a graphene *pnp* junction can be written

$$H = \sum_i(\varepsilon_i + \omega_i)a_i^\dagger a_i + \sum_{\langle i,j\rangle} t e^{i\phi_{ij}}a_i^\dagger a_j + \sum_{\langle\langle i,j\rangle\rangle} t' e^{i\phi_{ij}}a_i^\dagger a_j, \tag{21}$$

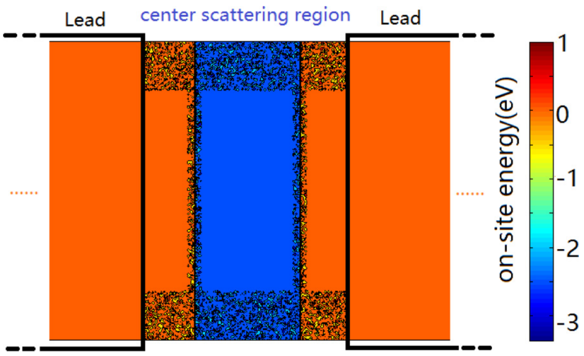

FIG. 2. This is a map of onsite energy for a random disorder configuration. The graphene *pnp* junction consists of the left and right *p* regions and the center *n* region. The center scattering region includes the center *n* region and a part of the left and right *p* regions. The disorder only exists in the center scattering region near the boundary of nanoribbon and *pn* interface.

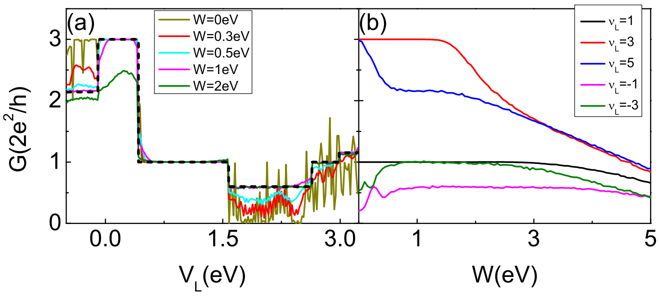

FIG. 3. (a) The conductance versus onsite energy V_L with different disorder strengths, while the theoretical conductance is given as black dashed line. (b) The conductance versus disorder strength with different onsite energy V_L (i.e., filling factors ν_L). The onsite energy V_L is 1.0, 0.3, -0.3, 2.2, and 2.8 eV, from upper to lower in the legend. The onsite energy V_G is fixed on 0.15 eV with the filling factor $\nu_G = 3$, and the magnetic field $\phi = 0.1$ for a hexagonal lattice.

where a_i ($a_i^\dagger$) annihilates (creates) an electron on carbon atom i, t and t' are the nearest- and second-nearest-neighbor hopping energies. In this paper, $t = 2.7$ eV and $t' = 0.2t$. The magnetic factor $e^{i\phi_{ij}}$ comes from Peierls substitution and $\phi_{ij} = \int_i^j \boldsymbol{A} \cdot d\boldsymbol{l}/\Phi_0$ where $\boldsymbol{A}$ is magnetic vector potential and $\Phi_0 = \hbar/e$ [45]. The onsite energy ε_i can be controlled by gate voltage, and ω_i is disorder potential. We set $\varepsilon_i = V_G$ in the left and right *p* regions due to a global gate which can control them in the experiment, and $\varepsilon_i = V_L$ in the center *n* region which can experimentally be tuned by a local gate. We take the disorder term $\omega_i = WR(i)$ where W denotes the disorder strength and $R(i)$ is a random factor drawn from the standard normal distribution. This is a short-range disorder and we will apply this type of disorder throughout this paper except in Figs. 5(c) and 5(d) where we are discussing the effect of long-range disorder. The simulated disorder distribution is shown in Fig. 2. Instead of adding disorder on the whole *pnp* region, disorder is added only near the boundary of nanoribbon and the interfaces of *pn* junctions (see Fig. 2), where the wave-function amplitude is most significant. In addition, if disorder exists in the middle of nanoribbon, it would lead the scattering among edge states on the upper and lower sides of the nanoribbon, which is significant in the simulated small system but strongly depressed in the experiment's large device. The Green's function of the whole system can be calculated from $G^r_{\text{sys}} = (E - H_{\text{cen}} - \Sigma^r_L - \Sigma^r_R)^{-1}$, with the Hamiltonian H_{cen} of the center scattering region. Here, the center scattering region includes the center *n* region and parts of the left and right *p* regions. The retarded self-energy $\Sigma^r_{L/R} = H_{cL/R} G^r_{\text{surf},L/R} H^\dagger_{cL/R}$, where $H_{cL/R}$ is the hopping Hamiltonian between the center region and the left/right leads and $G^r_{\text{surf},L/R}$ is the surface Green's functions which can be calculated numerically from Eq. (13). Our following researches are made in armchair graphene nanoribbon, whose primitive cell contains two layers. The results are almost the same for the zigzag ribbon.

In the ballistic regime, when different modes completely mix up, the conductance G of *pnp* device is given as [24]

$$\begin{aligned}
&\text{unipolar} \quad G = \frac{2e^2}{h}|\nu_L|, \quad |\nu_G| > |\nu_L| \\
&\text{unipolar} \quad G = \frac{2e^2}{h}\left(\frac{1}{|\nu_G|} - \frac{1}{|\nu_L|} + \frac{1}{|\nu_G|}\right)^{-1}, \quad |\nu_G| \leqslant |\nu_L| \\
&\text{bipolar} \quad G = \frac{2e^2}{h}\frac{|\nu_L \nu_G|}{|\nu_G| + 2|\nu_L|},
\end{aligned} \tag{22}$$

where $\nu_L, \nu_G = \cdots -3, -1, 1, 3 \ldots$ refer to the filling factor in the center *n* region and left/right *p* region, and the factor 2 comes from spin degeneracy. A numerical simulation of a 170-layer armchair *pnp* device is performed in this section. The *pnp* device is consisted of a 70-layer center *n* region and the 50-layer left/right *p* region, and each layer contains 200 atoms. Except where noted, this device is exerted in a strong vertical magnetic field whose magnetic index is $\phi = 0.1$ for a hexagonal lattice, and the onsite energy V_G in left/right *p* region is fixed to 0.15 eV, corresponding to filling factor $\nu_G = 3$ with Fermi energy $E = 0$ eV. In the numerical calculation, all curves are averaged over up to 1000 random configurations.

Figure 3(a) depicts the conductance G versus onsite energy V_L with different disorder strengths W, while the ideal conductance plateaus described by Eq. (22) is given as a black dashed line. At $W = 0$ eV, the conductance oscillates in bipolar regime, which is consistent with the experimental result [37]. The conductance plateaus emerge in the numerical simulation for the disorder strength W about from 0.5 to 1.5 eV, and these plateau values are well consistent with the theoretical predictions and experimental results [24]. This is clearer in Fig. 2(b) which shows the conductance G vs W, that every plot presents a plateau, which is exactly a theoretical value. In the unipolar regime (e.g., $\nu_L = 1$, 3, and 5), the conductance is large at the perfect *pnp* junction ($W = 0$). In the bipolar regime (that $\nu_L = -1$ and -3), G is small at $W = 0$ and raises with disorder in weak strength W, indicating a promotion to transport resulted from mode mixing. Then, the plateaus emerge at medium W. The plateaus for the lowest filling factor

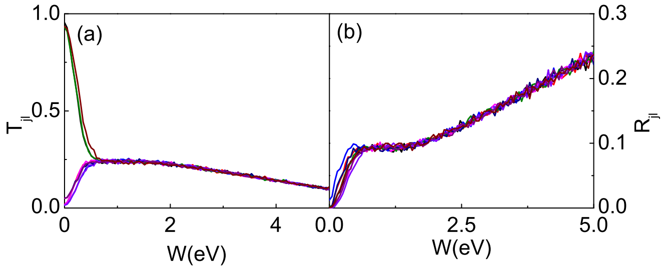

FIG. 4. Numerical simulation for (3,5,3) armchair graphene *pnp* junction. (a), (b) Show the nine elements of the transmission coefficient matrix T_{jl} and the nine elements of the reflection coefficient matrix R_{jl} versus the disorder strength W. In panel (a), the three curves with the value being about 1 at $W = 0$ are T_{11}, T_{22}, and T_{33}. While at $W \sim 0.6$ eV, nine curves in (a) and (b) converge together and they almost overlap in $W > 0.6$ eV. $V_L = -0.3$ eV and the other parameters are same as in Fig. 3.

(e.g., $\nu_L = 1$ and -1) can keep in a very large range of W, and the plateaus for higher filling factors are slightly narrow. All plateaus are succeeded by a decline regime because the system enters the insulator regime at strong W.

In order to show the mode mixing process specifically, a detailed inspection is taken on the effect of disorder at different filling factor ν_L. In the following context, (a,b,a) *pnp* junction symbolizes a graphene *pnp* junction with $\nu_G = a$ and $\nu_L = b$. We perform numerical simulations on (3,5,3), (3,1,3), and (3,−1,3) *pnp* junctions in sequence, corresponding to three different situations in Eq. (22). All parameters are the same as in Fig. 3, except for onsite energy V_L of the center n region and the disorder strength W.

At $\nu_L = 5$, the system is a (3,5,3) unipolar *pnp* junction. Because there are three incident modes in the left P terminal and three outgoing modes in the right p terminal, the transmission and reflection coefficient matrices T and R have $3 \times 3 = 9$ elements, and they as a function of the disorder strength W are shown in Fig. 4. In a perfect graphene device that $W = 0$ eV, the transmission matrix elements T_{11}, T_{22}, and T_{33} are close to 1. The other six elements of the transmission coefficient matrix and all nine elements of the reflection coefficient matrix R are close to 0. This indicates a high transparency of incident waves in perfect (3,5,3) *pnp* junction. There is no mode mixing and the incident electron goes forward along the original mode through the *pnp* junction. With the increasing of disorder strength W, T_{11}, T_{22}, and T_{33} reduce and the other six elements of the T matrix increase, and they converge together at about $W = 0.6$ eV. While W is larger than a critical disorder strength W_c (about 0.6 eV), nine elements of the T matrix are equal as well. All nine elements of the R matrix also increase with the increasing of W, and they are equal while W larger than a critical disorder strength W_c. The critical W_c for the R matrix is equal to one of the T matrix, indicating transmission modes and reflection modes mix up at the same disorder strength. In particular, a plateau emerges in the curves T_{jl}-W and R_{jl}-W at about 0.6 eV $< W <$ 1.5 eV [see Figs. 3(a) and 3(b)]. In this plateau, all nine transmission elements T_{jl} keep the same value and so do the nine reflection elements R_{jl}. For the unipolar junction with $|\nu_L| > |\nu_G|$, their plateau values are

$$T_{jl} = \frac{\nu_L}{\nu_G(2\nu_L - \nu_G)}, \tag{23}$$

$$R_{jl} = \frac{\nu_L - \nu_G}{\nu_G(2\nu_L - \nu_G)}. \tag{24}$$

For the (3,5,3) *pnp* junction with $\nu_L = 5$ and $\nu_G = 3$, $T_{jl} = \frac{5}{21}$ and $R_{jl} = \frac{2}{21}$. Notice that the same of all nine T_{jl} and R_{jl} indicate that an incident mode is either scattered into any one of three transmission modes in equal possibility, or into any one of three reflection modes in equal possibility, which clearly shows the occurrence of the perfect mode mixing. While W increases further, the system turns into the insulator regime, then all elements of the T matrix reduce and all elements of the R matrix increase. However, all elements of T and R matrices stay the same.

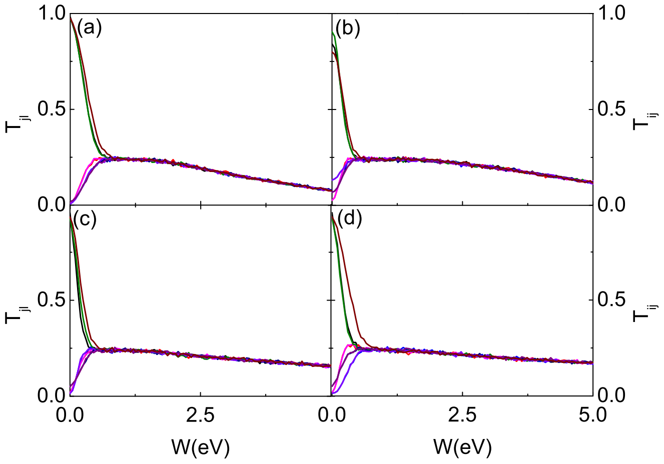

FIG. 5. Numerical simulation for (3,5,3) armchair graphene *pnp* junction. Each panel shows the nine elements of the transmission coefficient matrix T_{jl} versus the disorder strength W under different conditions. Panels (a) and (b) are under short-range disorder like in Fig. 4, while the magnetic flux $\phi = 0.05$ and 0.18, respectively. When the magnetic flux ϕ varies, the intervals between the Landau levels change also. In order to let the junction keep in the (3,5,3) case, the onsite energies are set $V_G = -0.6$ eV and $V_L = -0.3$ eV while $\phi = 0.05$, and $V_G = 0.3$ eV and $V_L = 0.9$ eV while $\phi = 0.18$. Panels (c) and (d) are under the common magnetic flux $\phi = 0.1$, while the disorder is long range with $\eta = 2$ and 5, respectively. The curve which converges slowest (dark red) in (c) and (d) stands for T_{11}. The other parameters are same as in Fig. 3.

Next, we consider the effect of the magnetic field on the mode mixing. Figures 5(a) and 5(b) show the nine elements of transmission coefficient matrix in a (3,5,3) unipolar junction with the magnetic flux $\phi = 0.05$ and 0.18, respectively. The similar results can be obtained. In a clean *pnp* junction that $W = 0$, T_{11}, T_{22}, and T_{33} have a large value with close to 1, and the other six elements of the T matrix are small. At a critical disorder strength W_c, all nine elements of the T matrix converge together and they are equal as well while $W > W_c$. These results clearly show the occurrence of the perfect mode mixing while $W > W_c$. The critical disorder strength $W_c = 0.8$ eV under $\phi = 0.05$ and $W_c = 0.55$ eV under $\phi = 0.18$. Together with the value $W_c = 0.6$ eV under $\phi = 0.1$ in Fig. 4, it comes to the conclusion that the critical disorder strength W_c slightly decreases with the increase of the intensity of the magnetic field. The larger the magnetic field is, the slower the decrease W_c is. These features can be qualitatively explained with the help of the cyclotron radius of the magnetic field. The large magnetic field makes the electron trajectory closer to the interfaces of the *pnp* junction and the boundary of the graphene nanoribbon, and then the edge modes overlap together in space. So, it is easy that the perfect mode mixing occurs.

Up to now, we only consider the short-range disorder. In this paragraph, let us investigate the mode mixing under long-range disorder. The strength of short- and long-range disorders can not be simply compared. In order to make them more comparable, for the long-range disorder case, we choose the form of the disorder term ω_i in the Hamiltonian [see Eq. (21)] as [46]

$$\omega_i = \sum_j \tilde{\omega}_j \exp\left(-|\boldsymbol{r}_{ij}^2|/2\eta^2\right)/A, \tag{25}$$

where η is the spatial correlation parameter, $|\boldsymbol{r}_{ij}|$ is the distance between carbon atoms i and j, and $\tilde{\omega}_j = WR(j)$ with the disorder strength W and the standard normal distribution $R(j)$. The normalization coefficient A is chosen as

$$A = \sqrt{\sum_i \exp\left(-|\boldsymbol{r}_{ij}^2|/\eta^2\right)}. \tag{26}$$

The sum in Eq. (26) is taken over an infinite graphene plane. Using this normalization, the variance of onsite energy is equal in short- and long-range disorders for an infinite graphene plane. Mode mixing procedure with long-range disorder is presented in Figs. 5(c) and 5(d). For all the range η, nine elements of the T matrix can converge together well while the disorder strength W is a larger critical disorder strength. This means that the perfect mode mixing can occur regardless of the short- and long-range disorders. With the increase of the range η, the convergence of transmission coefficient T_{11} is significantly slower than other coefficients. This indicates the robustness of the first edge mode and it is difficult to mix the first edge mode with others. From Figs. 6(a)–6(c), we can see that the first mode is closest to the boundary. On the other hand, under the long-range disorder, the disorder potential ω_i approximatively keeps it in the range η. So, it needs a larger disorder strength W to mix the first mode with others, in particular, for the large value η.

In the following, we take the magnetic flux $\phi = 0.1$ under the short-range disorder again. Figures 6(a)–6(l) show the space distribution of wave function $|\psi^{(lL)}|^2$ and the current density $j^{(lL)}$ for all three incident modes from the left lead at the (3,5,3) *pnp* junction, respectively. For the perfect graphene *pnp* junction with $W = 0$ eV, $|\psi^{(lL)}|^2$ and $j^{(lL)}$ for the first incident mode mainly distributes at the region very close to the lower boundary of the device and they almost are zero at the other region [see Figs. 6(a) and 6(d)], because that the first mode is the edge state of the first Landau level and it is very close to the boundary. For the second and third incident modes, the wave function $|\psi^{(lL)}|^2$ slightly emerges at the interface of the *pnp* junction [see Figs. 6(b) and 6(c)], but the reflection wave function and the reflection current density are very small still. These results clearly show the incident electron goes forward along the original mode through the perfect (3,5,3) *pnp* junction and the mode mixing does not occur. On the other hand, while in the presence of the disorder ($W = 0.5$ eV) the mode mixing occurs, all the three scattering states show much similarity. From Figs. 6(g)–6(i), one can clearly see that the wave-function distributions in the center regions for the three incident modes are almost the same. In addition, the current density $j^{(lL)}$ for all three incident modes is the same also [see Figs. 6(j)–6(l)]. This means that the perfect mode mixing not only makes that the incident electron has the equal probability to each outgoing (reflection) mode, but also makes the same current density in the whole scattering region for all incident modes.

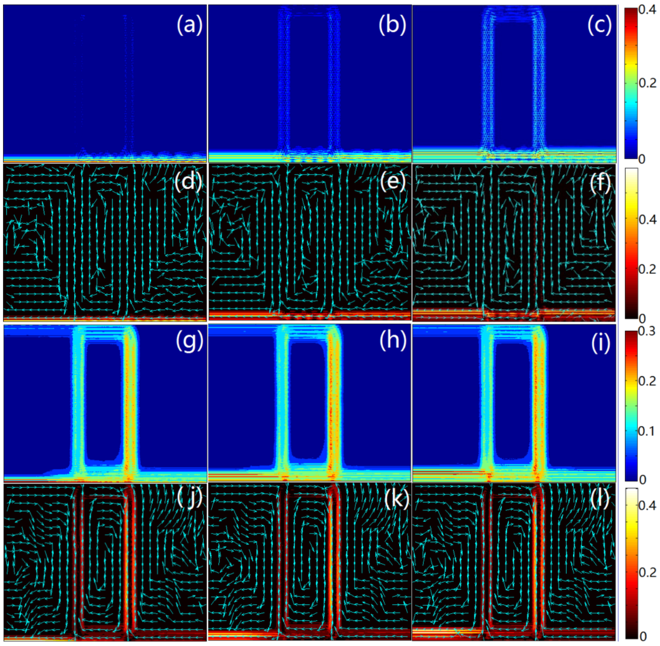

FIG. 6. The space distribution of the wave functions $|\psi^{(lL)}|^2$ [(a)–(c) and (g)–(i)] and the corresponding current density [(d)–(f) and (j)–(l)] of scattering states in (3,5,3) armchair graphene *pnp* junction. The color indicates the intensity of wave function and current, and the arrows in current density pictures indicate the orientation. Panels (a)–(f) are for the perfect *pnp* junction without disorder ($W = 0$ eV), where all the three scattering states are perfect conducting channel. The disorder strength at (g)–(l) is $W = 0.5$ eV. The columns from left to right are for the first, second, and third incident modes, respectively. $V_L = -0.3$ eV and the other parameters are same as in Fig. 3.

Next, let us study the (3,1,3) unipolar *pnp* junction. Since there is only one conducting mode in the center n region which is less than three modes in the left and right p regions, the conductance is decided by the filling factor $|\nu_L|$ of the center region. In this case, some works have shown that the mode mixing is absent and the conductance is usually $\frac{2e^2}{h}|\nu_L|$, except for in the insulator regime while at the very strong disorder W. Figures 7(a) and 7(b) show the nine elements of the transmission and reflection coefficient matrices as well as the total transmission and reflection coefficients versus the disorder strength W. The total transmission coefficient T is 1 and the total reflection coefficient R is 2 in a large range of W (from 0 to 2.6 eV), as expected. From the results of the total T and R, it shows that the carrier seems to flow ballistically through the *pnp* junction and the mode mixing seems to be unimportant. However, from the nine elements of T_{jl} and R_{jl}, they clearly show the occurrence of the mode mixing still. At the absence of the disorder ($W = 0$ eV), the T_{11} is very large and the other eight elements T_{jl} are very small [see Fig. 7(a)], which means that the incident electron from the first mode can well go forward along the same mode through the junction and the incident electron from the other mode is reflected back. With the increase of W, the T_{11} reduces and the other eight elements T_{jl} increase due to the mode mixing, although the total T keeps 1 still. They converge together at about $W = 0.8$ eV. Then, while $W > 0.8$ eV, all elements T_{jl} and R_{jl} are same. While W in the range of from 0.8 to 2.6 eV, T_{jl} and R_{jl} show the plateau with $T_{jl} = \frac{1}{9}$ and $R_{jl} = \frac{2}{9}$. These results clearly show the occurrence of the perfect mode mixing while 0.8 eV $< W <$ 2.6 eV.

Figures 7(c) and 7(d) show the fluctuation of each element and total of the transmission and reflection coefficients for the (3,1,3) *pnp* junction. Here, the fluctuation is defined as, e.g., $rms(T) = \sqrt{\langle T^2\rangle - \langle T\rangle^2}$ and $\langle\ldots\rangle$ is the average over the random disorder configurations. The fluctuations of the total transmission efficient T and total reflection efficient R are zero while W is less than 2.2 eV; this seems to show the ballistical transport and the mode mixing are absent. However, all elements of transmission and reflection matrices hold a nonzero fluctuation, although the sum of them has a zero fluctuation. This clearly indicates the occurrence of the mode mixing. In particular, at the perfect mode mixing case, the nine elements of T_{jl} and R_{jl} have the same fluctuations. They exhibit the plateau while 0.8 eV $< W <$ 2.6 eV. For the (3,1,3) *pnp* junction, the plateau value of fluctuation of T_{jl} is $\sqrt{5}/18$ and the plateau value of fluctuation of R_{jl} is $\sqrt{11}/18$.

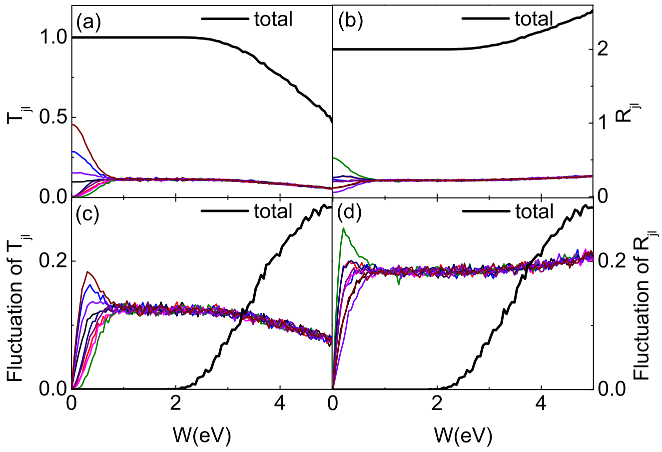

FIG. 7. Numerical simulation for (3,1,3) armchair graphene *pnp* junction. (a), (b) Present the nine elements of transmission and reflection coefficient matrices vs disorder strength W, respectively. Here, the total transmission and reflection coefficients, the sum of all nine elements, are shown also (see the black line). (c), (d) Show the fluctuation of each element and total transmission and reflection coefficients vs disorder strength W. Notice that the fluctuation of the total transmission (reflection) coefficient T (R) is not equal to the sum of the fluctuation of the nine elements T_{jl} (R_{jl}), although $T = \sum_{jl} T_{jl}$ ($R = \sum_{jl} R_{jl}$). $V_L = 1.0$ eV and the other parameters are same as in Fig. 3.

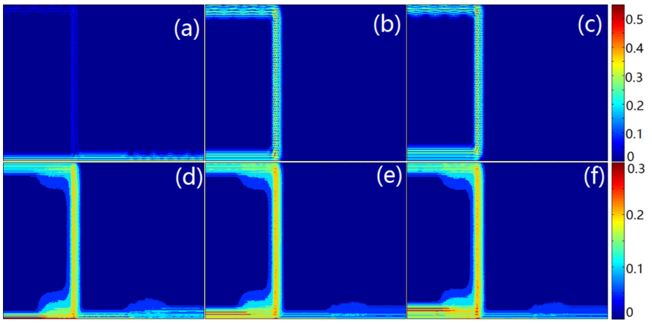

FIG. 8. The space distribution of the wave functions $|\psi^{(lL)}|^2$ of scattering states in (3,1,3) armchair graphene *pnp* junction. The color indicates the intensity of wave function. Panels (a)–(c) are for the perfect *pnp* junction without disorder ($W = 0$ eV), while the disorder strength at (d)–(f) is $W = 1$ eV. The columns from left to right are for the first, second, and third incident modes, respectively. $V_L = 1.0$ eV and the other parameters are same as in Fig. 3.

The space distributions of wave function $|\psi^{(lL)}|^2$ for three incident modes in the (3,1,3) *pnp* junction are shown in Fig. 8. At the disorder strength $W = 0$ eV, three scattering states are very different [see Figs. 8(a)–8(c)]. For the first incident mode, the wave function mainly distributes on the lower boundary, and it exhibits that this incident electron goes forward without backscattering. But, for the second and third modes, the incident electrons are mainly backscattered along the upper boundary. On the other hand, while $W = 1$ eV, three scattering states show well similarity [see Figs. 8(d)–8(f)], this indicates the occurrence of the perfect mode mixing, although the total transmission coefficient T is 1 still.

A bipolar *pnp* junction is formed by two *pn* junctions arranged back to back. Unlike in a unipolar *pnp* junction where exists conducting channel and has a large conductance at $W = 0$ eV, in a bipolar *pnp* junction *pn* interfaces block the conducting channel and the conductance usually is small at the absence of the disorder (see Fig. 3). In the bipolar junction, disorder can promote electron transport and increase the conductance due to mode mixing [33,47]. This can be seen in Fig. 3(b) where the conductances of $\nu_L = -1$ and -3 raise in weak disorder case. Figure 9 shows the nine elements of the transmission and reflection coefficient matrices versus disorder strength W for the (3,−1,3) bipolar *pnp* junction. At weak W, the nine elements of T and R matrices

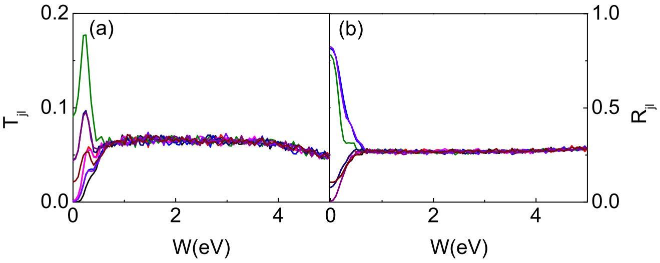

FIG. 9. (a), (b) Present the nine elements of transmission and reflection coefficient matrices vs disorder strength W in (3,−1,3) armchair graphene *pnp* junction, respectively. $V_L = 2.2$ eV and the other parameters are same as in Fig. 3.

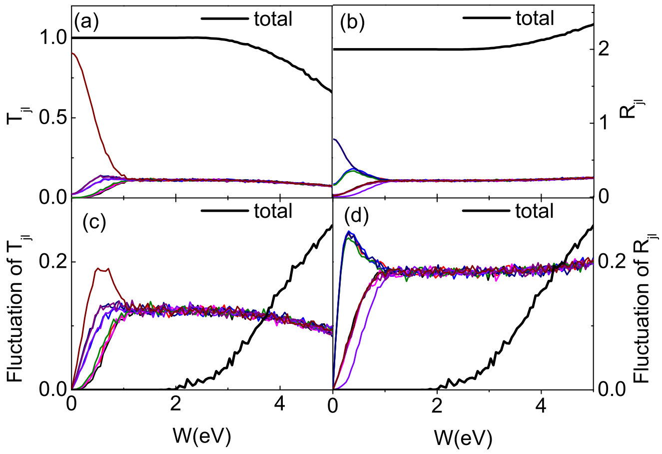

FIG. 10. Numerical simulation for (3,1,3) Stone-Wales edge-reconstructed zigzag graphene *pnp* junction. (a), (b) Show the nine elements of transmission and reflection coefficient matrices as well the total transmission and reflection coefficients vs disorder strength W. (c), (d) Show the fluctuation of each element and total transmission and reflection coefficients vs W. The parameters are same as in Fig. 7.

are very different. However, about at $W = 0.6$ eV, all nine elements of T (R) matrices well merge together. They are equal always for the larger W, and they exhibit the plateaus at the large range of $0.6 \text{ eV} < W < 3.5$ eV, which well indicates perfect mode mixing for $W > 0.6$ eV. The plateau values are $T_{jl} = \frac{|\nu_L|}{|\nu_G|(|\nu_G|+2|\nu_L|)}$ and $R_{jl} = \frac{|\nu_G|+|\nu_L|}{|\nu_G|(|\nu_G|+2|\nu_L|)}$. For the (3,−1,3) junction with $\nu_G = 3$ and $\nu_L = -1$, $T_{jl} = \frac{1}{15}$ and $R_{jl} = \frac{4}{15}$, which is well consistent with the numerical results in Figs. 9(a) and 9(b).

All these aforementioned numerical simulations are based on the armchair nanoribbon. We have also performed these numerical calculations in the *pnp* junction based on the zigzag nanoribbon, whose size matches the simulated armchair one, that means the simulated zigzag nanoribbon is also consisted of a 70-layer center n region and two 50-layer left and right p regions, and each layer contains 200 atoms. We have repeated all curves in Figs. 3–9, and obtained the same results.

In addition, this method can be applied in other materials. We choose an edge-reconstructed zigzag *pnp* junction, for example. Its boundary is reformed by Stone-Wales defects, that pentagon-heptagon pairs which often forms at the boundary of CVD-grown graphene [48]. Figure 10 presents the transmission and reflection coefficient matrices as well as their fluctuation versus disorder strength W. The results are very similar with the armchair nanoribbon case (see Figs. 7 and 10). The total transmission and reflection coefficients display the plateau beginning at $W = 0$ to 2.6 eV. But, the nine elements T_{jl} and R_{jl} are not equal at $W = 0$. They merge until $W = 0.6$ eV and then show the plateau for W from 0.6 to 2.6 eV. While at the plateau, the fluctuations of the total transmission and reflection coefficients are exactly zero. However, the fluctuations of the nine elements T_{jl} and R_{jl} are not zero, and they exhibit the plateau with the plateau values $\sqrt{5}/18$ for T_{jl} and $\sqrt{11}/18$ for R_{jl}. These indicate the occurrence of perfect mode mixing which is quite similar to the armchair *pnp* junction case.

IV. CONCLUSIONS

In summary, we have obtained extended transmission and reflection coefficient formulas in a two-terminal system by Sanvito and Lambert to the multiterminal system. These formulas can give the scattering wave function and the current density in the real space for a specific incident mode from an arbitrary terminal, as well as can give the transmission and reflection coefficients from a specific incident mode to an arbitrary outgoing mode. By using these formulas, we study electron transport through a graphene *pnp* junction. While at the perfect *pnp* junction, the elements of the transmission and reflection coefficient matrices are very different, and the space distribution of the scattering wave function for different incident modes has a large difference as well. But, they merge at the presence of disorder. While the disorder is stronger than a critical value, all elements of the transmission matrix are the same regardless of unipolar or bipolar junctions, so are all elements of the reflection matrix. At the suitable disorder, all elements of the transmission and reflection matrices show the plateau structure, as well the scattering wave function for the different incident modes are similar. These results clearly indicate the occurrence of perfect mode mixing. Moreover, the perfect mode mixing can occur regardless of the intensity of the magnetic field and the disorder nature. In particular, while the mode number in the center region is less than that in the left and right regions in the unipolar *pnp* junction, an interesting phenomenon occurs. Here, the fluctuation of the total transmission and reflection coefficients is exactly zero, which seems to indicate the ballistic transport. However, all elements of transmission and reflection matrices show the fluctuation and clearly mean the occurrence of the perfect mode mixing in this case also.

ACKNOWLEDGMENTS

We gratefully acknowledge the financial support from NBRP of China (Grant No. 2015CB921102), NSF-China under Grants No. 11274364 and No. 11574007.

---

[1] P. R. Wallace, Phys. Rev. **71**, 622 (1947).

[2] A. H. Castro Neto, F. Guinea, N. M. R. Peres, K. S. Novoselov, and A. K. Geim, Rev. Mod. Phys. **81**, 109 (2009).

[3] M. I. Katsnelson, K. S. Novoselov, and A. K. Geim, Nat. Phys. **2**, 620 (2006).

[4] K. S. Novoselov, V. I. Fal'ko, L. Colombo, P. R. Gellert, M. G. Schwab, and K. Kim, Nature (London) **490**, 192 (2012).

[5] A. Cresti, Nanotechnology **19**, 265401 (2008).

[6] J. R. Williams, L. DiCarlo, and C. M. Marcus, Science **317**, 638 (2007).

[7] F. Schwierz, Nat. Nanotechnol. **5**, 487 (2010).

[8] C.-H. Kim and C. D. Frisbie, J. Phys. Chem. C **118**, 21160 (2014).

[9] Y. M. Lin, A. Valdes-Garcia, S. J. Han, D. B. Farmer, I. Meric, Y. N. Sun, Y. Q. Wu, C. Dimitrakopoulos, A. Grill, P. Avouris, and K. A. Jenkins, Science **332**, 1294 (2011).

[10] N. N. Klimov, S. T. Le, J. Yan, P. Agnihotri, E. Comfort, J. U. Lee, D. B. Newell, and C. A. Richter, Phys. Rev. B **92**, 241301 (2015).

[11] S. Nakaharai, J. R. Williams, and C. M. Marcus, Phys. Rev. Lett. **107**, 036602 (2011).

[12] V. V. Cheianov, V. Fal'ko, and B. L. Altshuler, Science **315**, 1252 (2007).

[13] V. V. Cheianov and V. I. Fal'ko, Phys. Rev. B **74**, 041403 (2006).

[14] J. R. Williams and C. M. Marcus, Phys. Rev. Lett. **107**, 046602 (2011).

[15] J.-C. Chen, X. C. Xie, and Q.-F. Sun, Phys. Rev. B **86**, 035429 (2012).

[16] Y. Liu, R. P. Tiwari, M. Brada, C. Bruder, F. V. Kusmartsev, and E. J. Mele, Phys. Rev. B **92**, 235438 (2015).

[17] P. Rickhaus, P. Makk, M.-H. Liu, E. Tóvári, M. Weiss, R. Maurand, K. Richter, and C. Schöenenberger, Nat. Commun. **6**, 6470 (2015).

[18] T. Taychatanapat, J. Y. Tan, Y. Yeo, K. Watanabe, T. Taniguchi, and B. Özyilmaz, Nat. Commun. **6**, 6093 (2015).

[19] F. Amet, J. R. Williams, K. Watanabe, T. Taniguchi, and D. Goldhaber-Gordon, Phys. Rev. Lett. **112**, 196601 (2014).

[20] F. Amet, J. R. Williams, K. Watanabe, T. Taniguchi, and D. Goldhaber-Gordon, Phys. Rev. Lett. **110**, 216601 (2013).

[21] J. Velasco, Y. Lee, L. Jing, G. Liu, W. Bao, and C. N. Lau, Solid State Commun. **152**, 1301 (2012).

[22] J. Velasco, G. Liu, W. Z. Bao, and C. N. Lau, New J. Phys. **11**, 095008 (2009).

[23] M. F. Craciun, S. Russo, M. Yamamoto, and S. Tarucha, Nano Today **6**, 42 (2011).

[24] S.-G. Nam, D.-K. Ki, J. W. Park, Y. Kim, J. S. Kim, and H.-J. Lee, Nanotechnology **22**, 415203 (2011).

[25] D.-K. Ki, S.-G. Nam, H.-J. Lee, and B. Özyilmaz, Phys. Rev. B **81**, 033301 (2010).

[26] J. Baringhaus, A. Stöhr, S. Forti, U. Starke, and C. Tegenkamp, Sci. Rep. **5**, 9955 (2015).

[27] H. Liu, Y. Liu, and D. Zhu, J. Mater. Chem. **21**, 3335 (2011).

[28] E. C. Peters, E. J. H. Lee, M. Burghard, and K. Kern, Appl. Phys. Lett. **97**, 193102 (2010).

[29] A. F. Young and P. Kim, Nat. Phys. **5**, 222 (2009).

[30] Y. Xing, J. Wang, and Q.-F. Sun, Phys. Rev. B **81**, 165425 (2010).

[31] T. Low, Phys. Rev. B **80**, 205423 (2009).

[32] D. A. Abanin and L. S. Levitov, Science **317**, 641 (2007).

[33] W. Long, Q.-F. Sun, and J. Wang, Phys. Rev. Lett. **101**, 166806 (2008).

[34] B. Özyilmaz, P. Jarillo-Herrero, D. Efetov, D. A. Abanin, L. S. Levitov, and P. Kim, Phys. Rev. Lett. **99**, 166804 (2007).

[35] J. Velasco, G. Liu, L. Jing, P. Kratz, H. Zhang, W. Bao, M. Bockrath, and C. N. Lau, Phys. Rev. B **81**, 121407 (2010).

[36] G. Liu, J. Velasco, Jr., W. Bao, and C. N. Lau, Appl. Phys. Lett. **92**, 203103 (2008).

[37] S. Morikawa, S. Masubuchi, R. Moriya, K. Watanabe, T. Taniguchi, and T. Machida, Appl. Phys. Lett. **106**, 183101 (2015).

[38] N. Kumada, F. D. Parmentier, H. Hibino, D. C. Glattli, and P. Roulleau, Nat. Commun. **6**, 8068 (2015).

[39] S. Matsuo, S. Takeshita, T. Tanaka, S. Nakaharai, K. Tsukagoshi, T. Moriyama, T. Ono, and K. Kobayashi, Nat. Commun. **6**, 8066 (2015).

[40] J.-C. Chen, T. C. Au Yeung, and Q.-F. Sun, Phys. Rev. B **81**, 245417 (2010).

[41] J. Li and S.-Q. Shen, Phys. Rev. B **78**, 205308 (2008).

[42] S. Sanvito, C. J. Lambert, J. H. Jefferson, and A. M. Bratkovsky, Phys. Rev. B **59**, 11936 (1999).

[43] R. Landauer, IBM J. Res. Dev. **1**, 223 (1957).

[44] S. Datta, *Electronic Transport in Mesoscopic Systems* (Cambridge University Press, Cambridge, 1997).

[45] R. Peierls, Z. Phys. **80**, 763 (1933).

[46] S.-G. Cheng, H. Zhang, and Q.-F. Sun, Phys. Rev. B **83**, 235403 (2011).

[47] H. Schmidt, J. C. Rode, C. Belke, D. Smirnov, and R. J. Haug, Phys. Rev. B **88**, 075418 (2013).

[48] J. N. B. Rodrigues, P. A. D. Goncalves, N. F. G. Rodrigues, R. M. Ribeiro, J. M. B. Lopes dos Santos, and N. M. R. Peres, Phys. Rev. B **84**, 155435 (2011).